batteries

MDPI

Article

Lightweight Aircraft Battery Enclosures Made From 3-D Printed Continuous Fiber-Reinforced Composites

Meelad Ranaiefar [1], Amjad Almansour [1] and Mrityunjay Singh [2,*]

[1] NASA Glenn Research Center, Cleveland, OH 44135, USA; meelad.ranaiefar@nasa.gov (M.R.); amjad.s.almansour@nasa.gov (A.A.)
[2] Ohio Aerospace Institute, Cleveland, OH 44142, USA
* Correspondence: mrityunjay.singh-1@nasa.gov

Abstract

Advanced electric and hybrid-electric aircraft require battery enclosures that are both lightweight and structurally reliable. Continuous fiber-reinforced composites produced via additive manufacturing (AM) offer an effective solution by enabling tailored fiber architectures and reduced mass compared to traditional metallic housings. Continuous fiberglass reinforced (CFGR) composites were fabricated using fused filament fabrication and evaluated under tension, compression, and flexural loading to quantify mechanical performance. A full-scale, 12-inch-long battery enclosure was simulated, optimized, fabricated, and subjected to 100 h of cyclic cantilever bending to assess durability under representative service conditions. Results indicate that fiber orientation and architecture strongly influence mechanical response, with on-edge and concentric configurations exhibiting the highest strength and stiffness. The enclosure sustained repeated deflections of up to 7.65 mm without permanent deformation or cracking, confirming its suitability for installation in aircraft wing structures. These findings demonstrate the potential of continuous fiber AM to produce lightweight, structurally robust battery enclosures and establish a framework for integrating simulation-guided design with mechanical testing.

Keywords: additive manufacturing; electrified aircraft; battery enclosure; continuous fiber reinforcement

Check for updates

Academic Editors: Zhi Cao, Chris Mi and Naser Vosoughi Kurdkandi

Received: 2 September 2026
Revised: 10 October 2026
Accepted: 15 October 2026
Published: 18 November 2026

Copyright: © 2026 by the United States Government as represented by the Administrator of the National Aeronautics and Space Administration and Ohio Aerospace Institute. Licensee MDPI, Basel, Switzerland. This article is an open access article distributed under the terms and conditions of the Creative Commons Attribution (CC BY) license.

Notice for Copyrighted Information: This manuscript is a joint work of employees of the National Aeronautics and Space Administration and employees of Ohio Aerospace Institute under GEARS Contract/Grant No. 80GRC020D0003 with the National Aeronautics and Space Administration. The United States Government may prepare derivative works, publish, or reproduce this manuscript and allow others to do so. Any publisher accepting this manuscript for publication acknowledges that the United States Government retains a non-exclusive, irrevocable, worldwide license to prepare derivative works, publish, or reproduce the published form of this manuscript, or allow others to do so, for United States government purposes.

1. Introduction

The transition toward electrified and hybrid-electric aviation is creating new requirements for lightweight, structurally reliable systems. Energy storage is at the center of this effort, with batteries representing both a mass-critical and safety-critical subsystem. Structural enclosures for batteries must combine mechanical robustness, thermal stability, and resistance to damage with minimal weight penalty in order to preserve aircraft payload capacity and range. Traditionally, steel and aluminum alloys have been used for

electric vehicle battery pack enclosures due to their established manufacturing processes and structural performance, although their high mass is particularly restrictive for electric aircraft where weight directly affects flight performance. Previous studies have investigated the trade-offs between enclosure weight reduction and crashworthiness, as well as the influence of lightweight material substitution on electric vehicle design, motivating the exploration of alternative materials and manufacturing approaches [1,2]. Additive manufacturing (AM) of polymer composites with continuous fiber reinforcement offers a promising alternative by enabling lightweight, geometrically complex designs with tailored reinforcement placement [3–5]. However, the structural performance and suitability of these AM composites for aircraft battery enclosures require further evaluation.

Over the past three decades, AM has evolved from a prototyping tool to a group of processes capable of producing functional, end-use components [6]. By fabricating structures in a layer-by-layer sequence, AM enables the production of geometries that are otherwise difficult to achieve with conventional machining or casting methods, while also allowing for reduced material waste, part consolidation, and integration of multifunctional features. These characteristics are particularly attractive for aerospace, where lightweight structures with integrated functionality are highly valued.

Within the family of AM processes, fused filament fabrication (FFF) has emerged as one of the most widely used technologies, due in part to low material and equipment costs, as well as its adaptability for both research and industrial prototyping. In FFF, thermoplastic filament is melted and deposited along programmed toolpaths to construct the part layer by layer [7]. A variety of polymers have been demonstrated, including acrylonitrile butadiene styrene (ABS), polylactic acid (PLA), polycarbonate (PC), and polyamides such as nylon 6 [8,9]. Despite its accessibility and versatility, FFF suffers from notable performance limitations. The tensile strength of standard FFF prints ranged between 30–100% that of injection-molded equivalents, and mechanical anisotropy caused by raster alignment leads to weakened properties in directions orthogonal to filament deposition [10]. Ahn et al. [11] provided one of the earliest fundamental studies of this issue, reporting significant anisotropy in the tensile and flexural properties of fused deposition modeling ABS specimens, linked directly to fiber orientation and void content. Similar findings by Torrado and Roberson [12] emphasized delamination as a common mode of failure under tensile loading. These property deficiencies have meant that FFF primarily serves rapid prototyping or non-structural roles, rather than being adopted for primary load-bearing components in aerospace systems.

Efforts to improve the performance of FFF components have largely focused on optimizing processing parameters. Studies consistently show that build orientation, raster angle, layer thickness, and extrusion temperature strongly influence part bonding and mechanical response. For example, Es-Said et al. [13] reported that in ABS parts, a 0°raster notably improved ultimate tensile strength compared to other orientations, while Sood et al. [14] demonstrated through a statistical design of experiments (DoE) that optimized combinations of layer thickness, raster width, and orientation resulted in improved tensile, flexural, and impact strength. Similarly, Lambiase et al. [15] found that extrusion and print speed along with deposition pattern significantly impact interlayer adhesion. Additionally, a recent study of PLA components reported that build direction strongly affects tensile strength with vertical prints showing significantly lower strength than horizontal orientations, underlining persistent anisotropy within AM parts [16]. While parameter optimization has demonstrated value, such gains often remain incremental, and the mechanical properties of most FFF unreinforced polymers along with their utilization in high-performance areas continue to lag.

A more robust avenue of performance enhancement has been reinforcement of polymer matrices. Two main strategies include the incorporation of chopped short fibers into the filament and embedding of continuous fibers during printing. The first approach, using short-fiber reinforcement, has been commercialized in several high-performance filaments (e.g., carbon-filled or glass-filled nylons). Such composites may exhibit higher stiffness compared to neat polymer filaments, but the gains are limited due to fiber discontinuity and non-ideal fiber orientation in the extruded filament product. In fact, voids introduced by chopped fiber reinforcement, possibly due to poor adhesion with the matrix, may result in reduced rather than increased stiffness and compressive strength [17]. By contrast, continuous fiber reinforcement allows fibers to carry load over large distances and enables stiffness and strength increases over unreinforced polymer AM parts. Recent reviews of AM for fiber-reinforced composites consistently highlight that continuous fiber systems hold the greatest promise for closing the performance gap between 3D-printed parts and conventional layup or molding techniques [18,19].

Continuous fiber deposition in AM has been demonstrated via several technical routes. One approach is in-nozzle impregnation, in which a continuous fiber (carbon, glass, or aramid) is pulled through a molten thermoplastic in the nozzle and deposited onto the build platform. An alternative is coextrusion, in which thermoplastic filaments and pre-impregnated fiber tows are printed in a coordinated manner to produce a bonded structure. Blok et al. [20] conducted a systematic investigation of continuous fiber AM, fabricating composite coupons reinforced with either continuous and short carbon fibers in a nylon matrix. Results showed tensile modulus and strength improved by more than an order of magnitude compared to short fiber reinforced nylon, demonstrating increased load-carrying ability and performance. Similarly, Justo et al. [21] investigated long fiber reinforcement by 3D printing and reported substantial improvements in stiffness and strength, though also highlighting the importance of layup strategy and fiber-path optimization in achieving robust results. Caminero et al. [22] evaluated continuous-fiber AM under impact loading conditions, showing that reinforced specimens displayed higher damage resistance and energy absorption compared to unreinforced prints.

Despite the progress, major knowledge gaps remain. First, most of the literature has emphasized monotonic tensile or flexural properties, whereas compressive behavior and fatigue resistance have received comparatively little attention. These properties are particularly critical in thin-walled enclosures, housings, and shells where local buckling and cyclic loading dominate. Second, studies typically focus on coupons or small-scale specimens rather than full-scale components. For aerospace adoption, it is vital not only to measure coupon-level properties but also to evaluate durability under simulated operational loads, including cyclic bending or vibration. Third, the influence of multiple parameters including orientation, volume fraction, and reinforcement distribution remains underexplored.

The present work aims to contribute to this emerging knowledge base by conducting a systematic investigation of 3D-printed polyamide 6 (PA6) reinforced with continuous glass fibers. A design of experiments methodology was adopted to evaluate the combined effects of fiber orientation and reinforcement distribution on tensile, compressive, and flexural performance. In addition to small-scale coupon testing, a full-scale twelve-inch enclosure representative of a battery housing was fabricated and subjected to 100 h of cyclic flexural loading to assess durability under service-representative conditions. By combining detailed coupon-level mechanical data with a structural demonstration at scale, this study seeks to advance the understanding of continuous fiber-reinforced AM and to provide quantitative insights enabling its application in lightweight and reliable enclosures for electric and hybrid-electric aircraft.

2. Materials and Methods

2.1. 3D Printer

A Markforged Mark Two 3D-printer (Markforged, Watertown, MA, USA) was used to fabricate specimens and the full-scale battery housing. It is a fused filament fabrication (FFF) printer capable of manufacturing high-strength parts through continuous fiber reinforcement technology. This is achieved by utilizing two nozzles, one which extrudes filament onto a print bed to build up a component layer by layer and a second to incorporate the continuous fiber reinforcement within each layer. This is advantageous for printing multi-functional and multi-material components. Although print parameters including nozzle temperature and speed are preset for specific materials to produce reliable high-quality prints, parameters such as material, fiber placement, part orientation, layer height, roof and floor layers, fill density, and fill pattern may be modified to produce tailored components for targeted applications.

2.2. Materials

Based on the module requirements and in-house 3D-printing capabilities, a high-strength high-temperature fiberglass (HSHT FG) reinforcement material was chosen alongside a base matrix of Onyx (nylon and chopped carbon fiber composite) for fabrication of the battery housing through the FFF 3D-printer. The HSHT FG is a continuous fiber reinforcement that can be integrated within the layers of a 3D-printed component, providing a substantial boost to tensile and flexural strength, while also providing a substantial heat deflection temperature. Table 1 provides a summary of these material properties, as well as density and thermal conductivity, for HSHT FG and Onyx. For comparison, carbon fiber reinforcement and conventional 6061 Aluminum are included as well.

Table 1. Material properties for aluminum, Onyx, HSHT FG, and carbon fiber. HDT—heat deflection temperature. Aluminum tensile modulus used for flexural modulus. Data from [23–27].

Material	Density [g/cm^3]	Thermal Conductivity [W/mK]	Tensile Strength [MPa]	Flexural Strength [MPa]	Flexural Modulus [GPa]	HDT [°C]
6061Aluminum	2.7	151–202	124–290	124–290	69	585 (melt)
Onyx	1.2	0.95	40	71	3	150
HSHTFG	1.5	0.05	600	420	21	150
CarbonFiber	1.4	8–10.45	800	540	51	105

Based on these properties, Onyx and HSHT FG demonstrate a 55.6% and 44.4% reduction in density relative to aluminum, respectively. Therefore, a significant weight reduction could be realized by integrating HSHT FG and Onyx in the fabrication of a composite module, while also demonstrating enhanced mechanical performance. Additionally, Onyx and HSHT FG have negligible thermal conductivity relative to Aluminum, allowing for the isolation of the module from its surrounding environment and the controlled thermal management of battery packs through an intentional and informed design approach. Although thermal management performance is not evaluated in the current work, this is an important design feature to consider in follow-on activities.

2.3. Modeling Software

Additive manufacturing for aircraft applications requires confidence in the structural performance and reliability of fabricated components. To support this, the Markforged platform provides the Eiger software v4.2.7, which integrates slicing, simulation, and optimization tools for continuous fiber reinforced architectures. In this workflow, a

computer-aided design (CAD) model generated in SolidWorks (v2023, Dassault Systems, Vélizy-Villacoublay, France) is uploaded into Eiger and configured to meet design objectives.

The process incorporates simulation tools that model the unique continuous fiber reinforcement achievable through FFF. As shown in Figure 1, the user defines boundary conditions by specifying anchor points and representative loading scenarios. The software evaluates the design against user-defined criteria such as maximum allowable deflection and desired safety factor. Simulation outputs include predicted part stiffness, critical stress locations, and a corresponding safety factor. However, it should be noted that the Eiger simulation framework functions as a black box where the internal models, assumptions, and algorithms are proprietary and not accessible to the user. Due to software limitations, only Onyx and carbon fiber reinforcement can be simulated. Additionally, a slightly raised region, providing boundary constraints for the applied load, was added to the model for simulation.

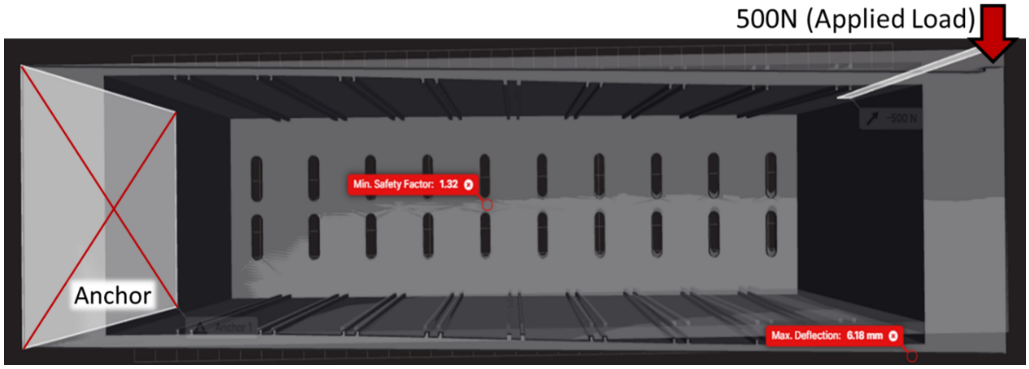


Figure 1. Simulated component in Eiger software. An anchor point and applied load are designated, and a predicted maximum deflection and minimum safety factor are output.

Design parameters available for optimization include fiber placement and routing, part orientation, matrix material, layer height, wall and floor thickness, fill density, and infill pattern. The slicer then generates fiber-reinforced toolpaths based on these inputs. A single simulation can validate whether performance criteria are met, while an optimization function explores multiple configurations to identify alternative print strategies that balance manufacturability and structural integrity. Once the optimal architecture is selected, the configuration is exported as an STL file and sent directly to the Markforged 3D printer for fabrication.

2.4. Battery Enclosure Design

Although numerous design features are possible, certain aspects of the module design were constrained based on battery pouch cell dimensions, testing criteria, and AM capabilities with the materials of interest. Battery pouch cell dimensions of 14.1 cm × 5.05 cm × 0.61 cm dictated the minimum slot dimensions for each pouch cell within the module. To account for the thermal management layering scheme that will be incorporated around each cell in future work, additional width and height are required to accommodate the battery cell and thermal management materials. Additionally, a tight fit is desired to induce a small compressive force onto the batteries, a common practice to improve the performance of these pouch cells. For these reasons, an internal pouch cell compartment of dimensions 14.6 cm × 6.99 cm × 2.42 cm was used. Illustrated in Figure 2, a three pouch cell design had dimensions 15.2 cm × 8.36 cm × 7.62 cm. Additionally, slots were incorporated into the front face of the module, allowing for the pouch cell tabs to protrude for connective access to the pouch cells. These slots also served as orifices for battery generated gases to escape the internal compartments and reduce the internal pressure build-up.

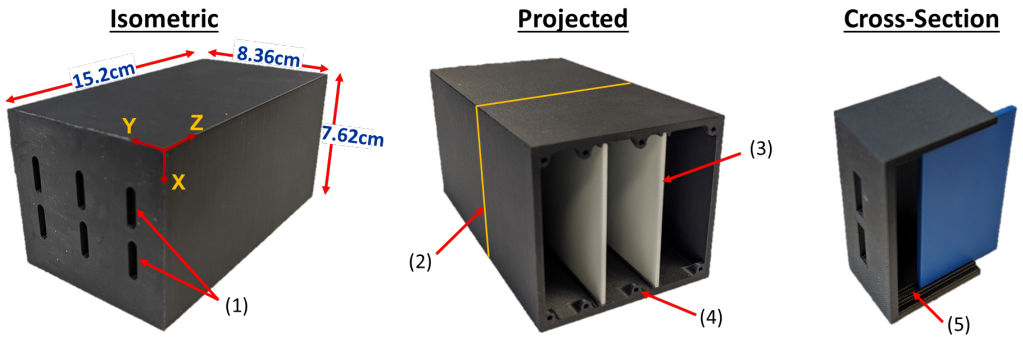


Figure 2. Schematic of 3D-printed battery housing module and key features: (1) slots for battery tabs; (2) concentric fiber reinforcement; (3) separator panels; (4) heat sink mechanical interface; (5) groove for dividing panels.

For the housing to accommodate a range of battery pouch cells for targeted applications, the design also leveraged a simple approach for modularity through appending additional compartments adjacent to one another, each separated by an ultra-high-temperature high-strength SG-200 fiberglass panel (Röchling Glastic Composites, Cleveland, OH, USA) with dimensions 6.99 cm × 0.159 cm × 14.9 cm. These panels would be inserted into grooved channels located along the top and bottom face of the module and incorporated into the 3D-printed design. These panels are situated with a tight fit within the groove and pressed against the front end of the module. By not rigidly attaching to the outer casing, these panels will be able to absorb mechanical stresses and damage induced by battery expansion and thermal runaway while reducing stress on the casing. On the rear, the dividing panels extend to be in-plane with a set of screw holes incorporated into the AM design. These features allow for a heat sink to be mechanically fastened flush to the rear of the module, providing a means for passive heat dissipation.

The 3D-printed enclosure consisted of 1524 layers, with 100% solid infill, designed to manage the thermo-mechanical stresses the system would experience. This is achieved by incorporating HSHT FG continuous reinforcement throughout the 3D-printed layers. It should be noted that one requirement for printing with this continuous fiber reinforcement, imposed by Eiger, is a minimum wall thickness of 0.279 cm, for which the current design has a wall thickness of 0.318 cm across all walls. Additionally, a smooth print finish is achieved by printing four floor layers, four ceiling layers, and two wall layers with only Onyx material serving as a shell along any exposed surface. In the current module, the slotted face is placed against the print bed with the open face extending up the Z-axis, in the print direction. This removes the need for wall supports during the print, reducing both print time and cost. Additionally, as illustrated in Figure 3, layers 1–4 of the print are the floor layers and contain only Onyx material. Layers 5–28 are then reinforced by two concentric rings of HSHT FG along both the perimeter of the module face and the slots, while layers 29–32 serve as ceiling for the slotted wall and have only a single concentric ring of HSHT FG continuous reinforcement around the perimeter of the module. This is shown in Figure 3B,C, respectively, where HSHT FG is depicted in orange. Layers 29–32 maintained this single ring of concentric reinforcement due to the continued extension of this region, serving as the 0.318 cm thick walls, through the remaining print layers. This is demonstrated in Figure 3D,E with layers 33–1520, where HSHT FG reinforcement remains constant after the screw holes are constructed on the module with layers 1438–1520. Shown in Figure 3F, layers 1521–1524 contain only Onyx and form the ceiling of the casing's four solid walls.

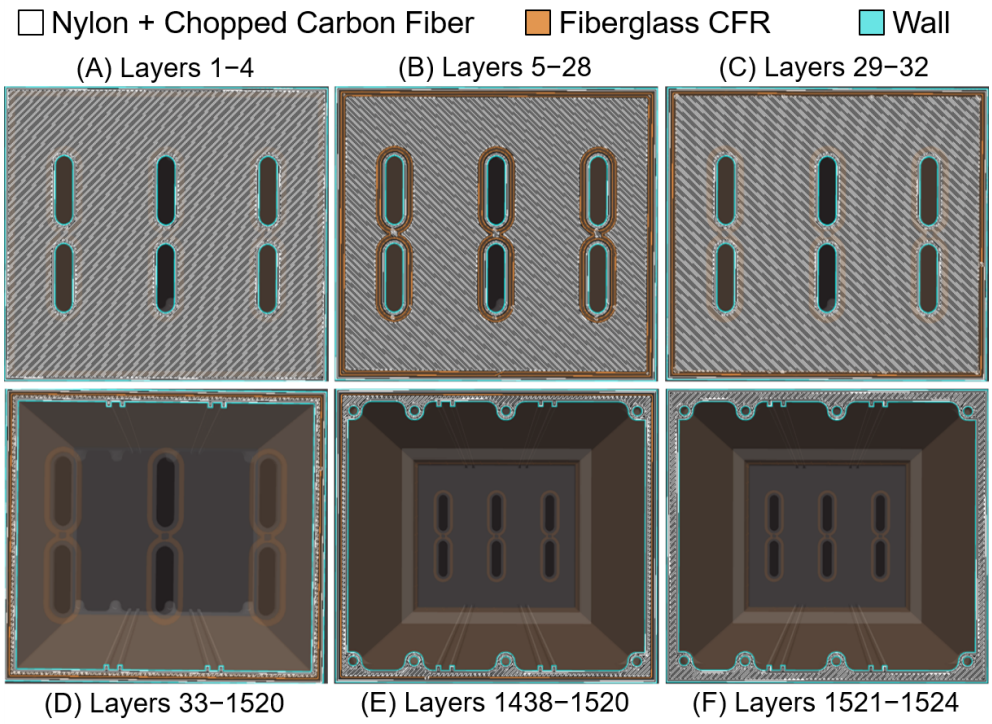


Figure 3. Architecture of battery enclosure at different cross-sections. White represents Onyx, orange represents continuous fiber reinforcement (CFR), and blue represents walls. (**A**) Layers 1–4; (**B**) Layers 5–28; (**C**) Layers 29–32; (**D**) Layers 33–1520; (**E**) Layers 1438–1520; (**F**) Layers 1521–1524.

For mechanical performance evaluation of the battery enclosure, the design was scaled to fabricate an expanded ten-pouch cell module. The 3D-printed test article, shown in Figure 4, incorporated a slight modification to accommodate gripping by the test fixture while housing ten pouch cells for cantilever bend fatigue testing, further discussed in Section 2.5.4. To this end, the mechanical test module measured 14.6 cm × 7.62 cm × 32.1 cm and included 2.54 cm solid end blocks on either side of the pack. These end blocks provided sufficient surface area for gripping and load application during testing. For clarity, the dividing panels and heat sink are not included in the mechanical testing module, as they were not intended to serve as structurally integral components.

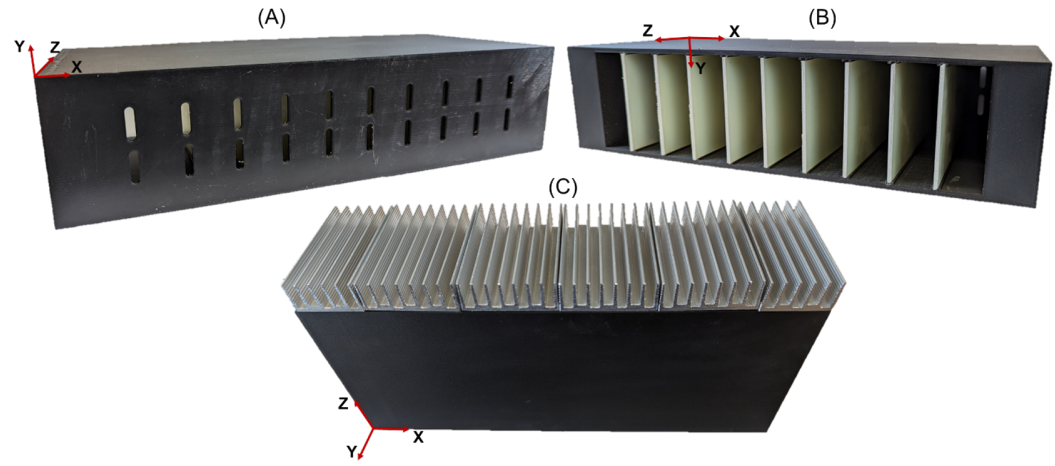


Figure 4. Battery enclosure designed to accommodate ten pouch cells: (**A**) slotted face; (**B**) open face; (**C**) example of incorporated heat sink.

2.5. Mechanical Testing

The mechanical evaluation of CFGR composite architectures was carried out through compression, tension, and flexural strength testing. As shown in Figure 5, specimens were fabricated in two orientations relative to the build plate, flat and on-edge. In the flat orientation, the specimen thickness corresponded to the build (z) axis, while in the on-edge orientation, the thickness was aligned with the x-axis and the width with the z-axis. In addition, cantilever bend fatigue testing was performed on a 10-pouch cell battery enclosure (batteries not included due to lab-safety restrictions). Further details for each test are provided in Sections 2.5.1–2.5.4.

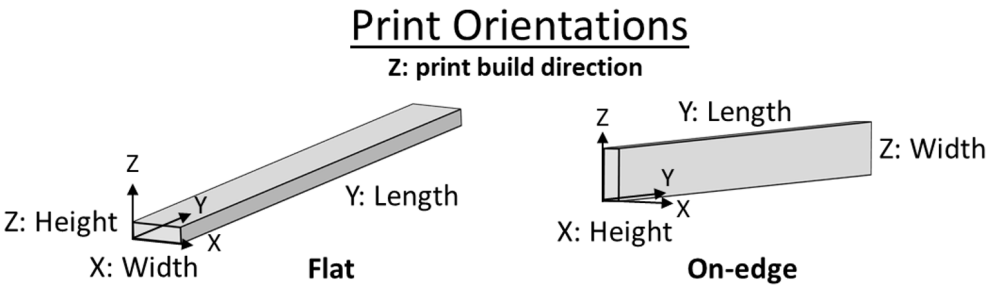


Figure 5. Flat and on-edge print orientation for test specimens.

Experimental uncertainty was quantified using the SciPy (v1.17.1) package in Python (v3.13.9). The 95% confidence intervals, $CI_{95\%}$, were calculated using Student's t-distribution according to

$$CI_{95\%} = \bar{x} \pm t_{0.975,n-1} \frac{s}{\sqrt{n}}, \quad (1)$$

where $\bar{x}$ is the sample mean, s is the sample standard deviation, n is the sample size, and $t_{0.975,n-1}$ is the critical value of Student's t-distribution with $n-1$ degrees of freedom. The 95% confidence intervals are presented in the corresponding figures to characterize the uncertainty in the estimated mean mechanical properties and facilitate comparison among the different fiber architectures.

Specific CFGR architectures selected for mechanical evaluation are shown in Figure 6. Flat-orientation prints included concentric reinforcement with either 2 or 5 fiberglass (FG) rings, fiber placement transverse to the loading direction, and an Onyx-only configuration, with fibers oriented transverse to the loading direction (precisely ±45° due to Eiger software restrictions). All specimens had 4 solid top and bottom Onyx layers, leaving 22 and 119 layers for the designated flat and on-edge CFGR architectures, respectively.

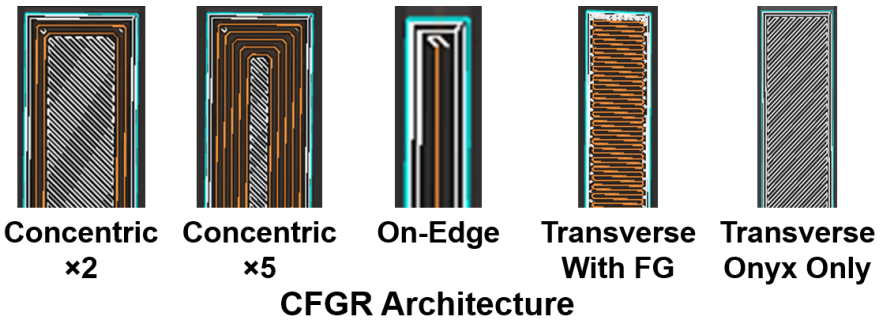


Figure 6. 3D-printed architectures for mechanical testing. White—onyx; orange—continuous fiberglass reinforcement (CFGR); blue—walls.

2.5.1. Compression Testing

Compression testing was performed in accordance with ASTM D6641 to determine the compressive strength and modulus of the CFGR composite architectures [28]. A typical test setup is shown in Figure 7. Specimens were designed with length, width, and thickness dimensions of 5.5 in. × 0.5 in × 0.12 in (139.7 mm × 12.7 mm × 3 mm), respectively, and were fitted with 2.5 in (63.5 mm) tabs. The tabs increased the load-bearing area at the grips, reducing stress concentrations and protecting the specimen from damage. Specimen dimensions were measured three times with calipers and averaged to determine cross-sectional area for stress calculations. Tests were conducted on an Instron Universal Testing Machine (UTM; Instron, Norwood, MA, USA) with a 50 kN load cell and a combined loading compression (CLC) fixture (Wyoming Test Fixtures, Salt Lake City, UT, USA).

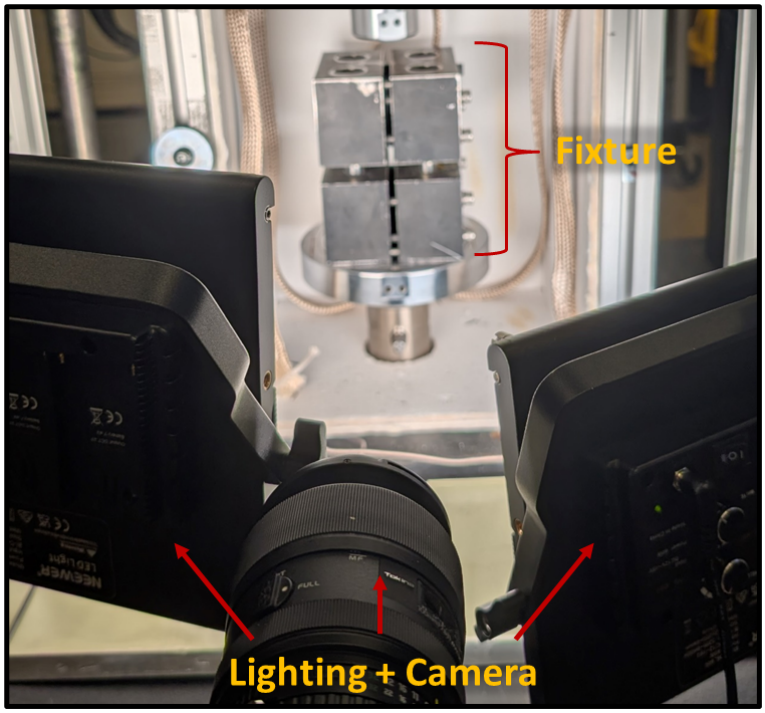


Figure 7. Experimental setup for compression testing with lighting and camera for DIC.

To facilitate digital image correlation (DIC), specimens were coated with white paint and speckled with black to create a reference pattern. Specimens were then oriented with a shim and secured in the CLC fixture using bolts tightened to 2.82 N·m. A 12.7 mm gauge section was left exposed to induce failure, and load was applied axially at a cross-head displacement rate of 1.27 mm/min. A DIC system (Correlated Solutions, Irmo, SC, USA) with a FLIR Grasshopper 3 camera (Teledyne FLIR LLC, Wilsonville, OR, USA), dedicated lighting, and an acquisition rate of 5 Hz was used to monitor deformation. Recorded images were processed using VicSnap (v9) and Vic2D (v7) software (Correlated Solutions) to quantify strain as well as bending percentage during loading, providing a measure of alignment and uniformity in the compression response.

Stress, σ, was calculated using:

$$\sigma = \frac{F}{A} \tag{2}$$

where F is the applied load and A is the cross-sectional area. Young's modulus E was determined from the linear elastic region of the stress–strain response, where ϵ is strain, using DIC data:

$$E = \frac{\sigma}{\epsilon} \tag{3}$$

The architectures investigated included 2× and 5× concentric, on-edge, transverse with FG reinforcement, and transverse Onyx-only, with five specimens tested per configuration.

2.5.2. Tensile Testing

Tensile testing was performed in accordance with ASTM D3039 to determine the ultimate tensile strength and Young's modulus of the CFGR composite architectures [29]. A typical test setup is shown in Figure 8. Specimens were designed with length, width, and thickness dimensions of 10 in × 0.5 in × 0.12 in (254 mm × 12.7 mm × 3 mm), respectively, and were fitted with 2.5 in (63.5 mm) tabs on both sides.

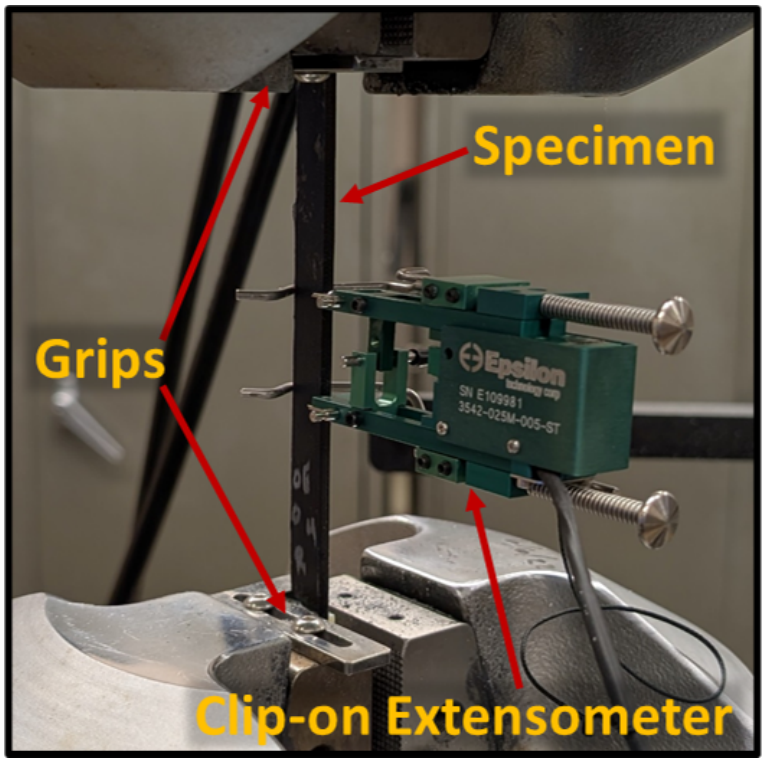


Figure 8. Experimental setup for tension testing with clip-on extensometer.

Tests were conducted on an Instron Universal Testing Machine (UTM) equipped with a 100 kN load cell and pressure-actuated grips set to 750 psi to avoid crushing the tabbed regions. A clip-on extensometer (Model 3542, Epsilon Technology Corp., Jackson, WY, USA) was mounted across the midpoint of the specimen gauge section to measure elongation and calculate strain. Specimen dimensions were measured three times with calipers and averaged to determine cross-sectional area for stress calculations. Specimens were gripped approximately 63.5 mm from each end and tested at a displacement rate of 2 mm/min until failure. Stress was calculated using Equation (2) and Young's modulus was determined from extensometer data using Equation (3).

The architectures investigated included 2× and 5× concentric, on-edge, transverse with FG reinforcement, and transverse Onyx-only, with five specimens tested for each configuration.

2.5.3. Flexural Strength Testing

Flexural strength testing was performed in accordance with ASTM D790 to determine the bending strength and tangent modulus of the continuous fiberglass reinforced (CFGR) composite architectures [30]. A typical test setup is shown in Figure 9. Specimens were designed with length, width, and thickness dimensions of 4.5 in × 0.5 in × 0.12 in (114.3 mm ×

12.7 mm × 3 mm), respectively. Specimen length, width, and thickness were measured three times with calipers and averaged to determine cross-sectional area for stress calculations.

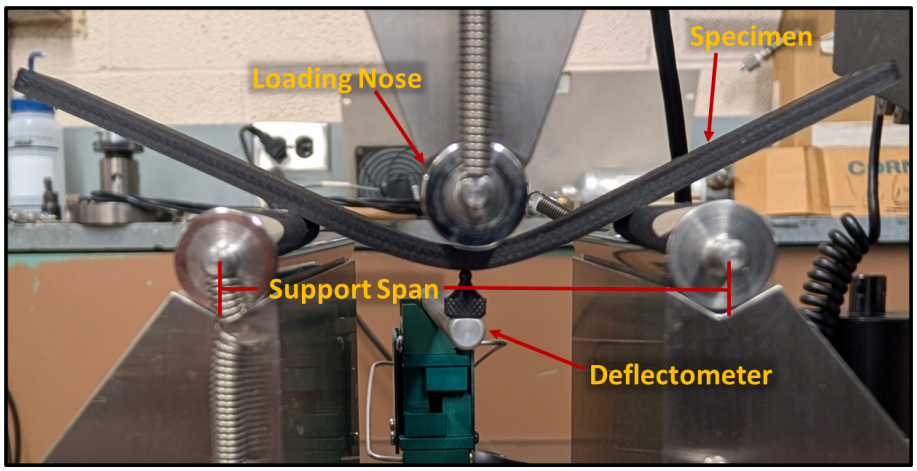


Figure 9. Experimental setup for flexural testing.

Tests were conducted on an Instron UTM equipped with a 2 kN load cell and a three-point bending fixture. The span length between supports was set at 44 mm, and load was applied at a constant crosshead displacement rate of 13 mm/min until failure. A deflectometer was mounted at the midpoint of the gauge section to measure deflection and calculate strain.

Flexural stress, σ_f, was calculated using:

$$\sigma_f = \frac{3FL}{2bd^2} \tag{4}$$

where F is the applied load, L is the support span, b is the specimen width, and d is the specimen thickness. Tangent modulus, E_f, was determined by

$$E_f = \frac{L^3 m}{4bd^3} \tag{5}$$

where m is the slope of the load–deflection curve's initial linear region.

The architectures investigated included on-edge, transverse with FG reinforcement, and transverse Onyx-only, with three specimens tested per configuration.

2.5.4. Cantilever Bend Fatigue of Battery Enclosure

Since the battery enclosure will likely be rigidly attached to an aircraft wing interior, it must withstand frequent bend-induced deflections without irreversible damage or load transfer to the batteries, regardless of the outer casing strength. To evaluate this, a cantilever bend fatigue experiment was designed and implemented. The setup used an Instron 55R4502 electromechanical frame with a 10 kN load cell to apply load at the top front face of the module, while deflection was measured on the bottom front face using an Epsilon Model 3540 deflectometer (±4 mm range, Epsilon Technology Corp., Jackson, WY, USA). An L-shaped extruded aluminum fixture rigidly secured the rear of the outer casing to the Instron frame, as shown in Figure 10. The loading rate was displacement-controlled at a rate of 0.5 mm/min with no dwell times.

The battery enclosure is shown mounted in the cantilever bend fatigue fixture and rigidly clamped to the extruded aluminum frame at the back using C-clamps. An aluminum bar, notched to seat a steel ball, was placed across the top front surface of the enclosure. The combination of the steel ball and notched bar ensured uniform transfer of the mechanical load from the Instron machine to the casing while maintaining proper alignment.

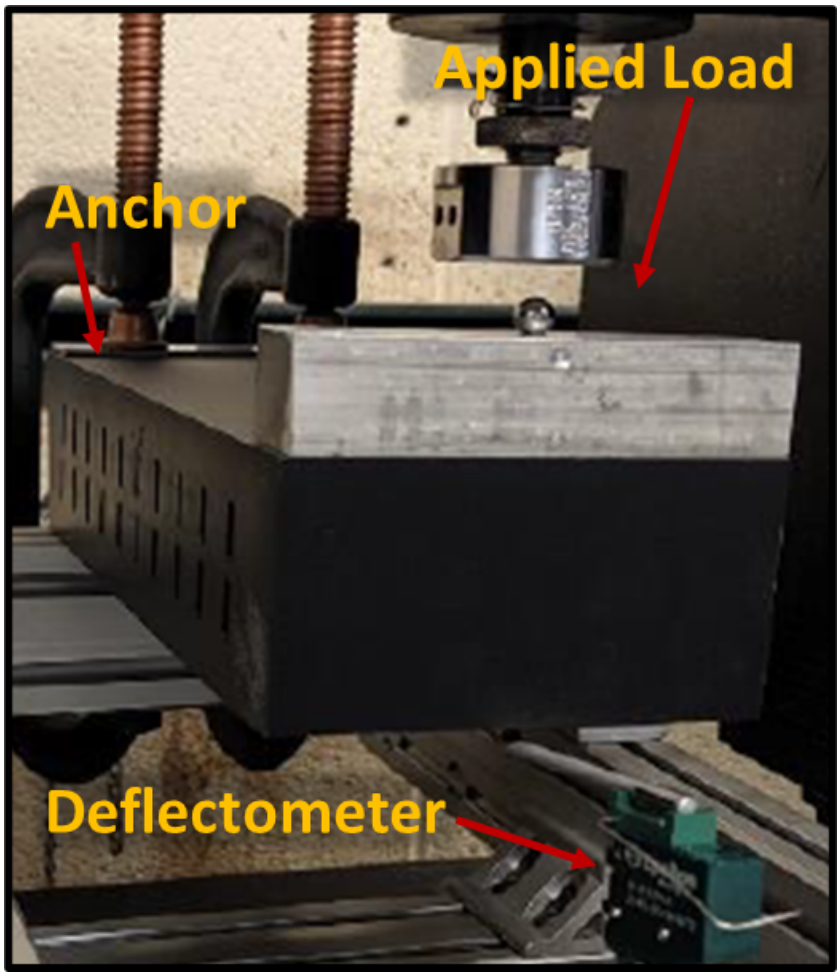


Figure 10. Battery housing prepared for cantilever bend fatigue test with one end anchored and load applied at the opposite end.

3. Results and Discussion

3.1. Compressive Behavior

Compressive stress and Young's modulus results are presented in Figure 11A and 11B, respectively. The concentric ×5 architecture exhibited the highest ultimate compressive stress at 128.1 MPa, followed by an equivalent performance from concentric ×2 at 65.58 MPa and on-edge at 65.28 MPa. These architectures had a greater proportion of CFGR aligned with the loading direction compared to the transverse FG and Onyx-only configurations, which achieved 49.99 MPa and 37.51 MPa, respectively, contributing to their lower compressive strength. The Young's modulus showed the same trend, with the concentric ×5 architecture achieving the highest value of 13.09 GPa, while the Onyx-only configuration had the lowest at 1.47 GPa. These results highlight the critical role of fiber orientation and alignment in efficiently transferring compressive loads through the CFGR matrix, directly influencing both stiffness and ultimate strength, and demonstrate the significant performance enhancement achievable compared to a baseline Onyx only configuration.

In accordance with ASTM D6641, the bend percentage of specimens under compression was evaluated to confirm compliance with the 10% threshold. Using DIC and Vic2D software, virtual extensometers were placed on the specimens to quantify bending. Figure 12 shows that, for all tests, the bend percentage remained within the 10% limit at the point of failure, confirming the validity of the results. Some variability was observed during initial loading due to noise, but this stabilized as the applied load increased.

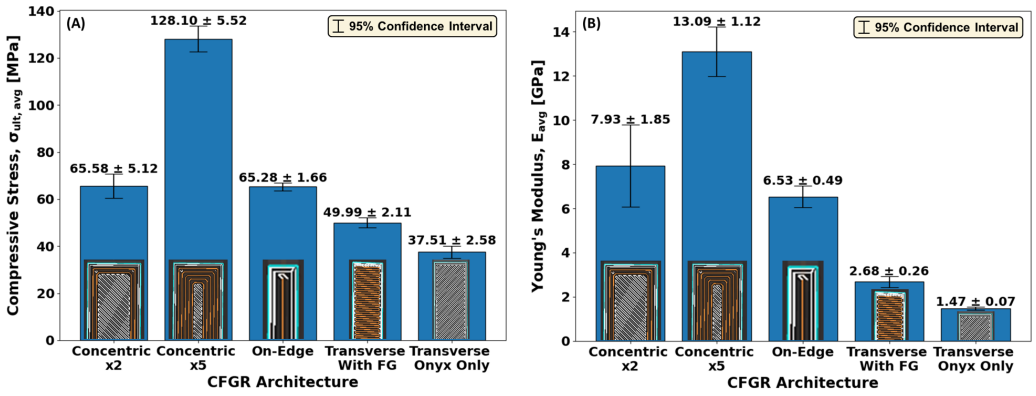


Figure 11. Compressive stress (**A**) and modulus (**B**) results for continuous fiberglass reinforced (CFGR) architectures.

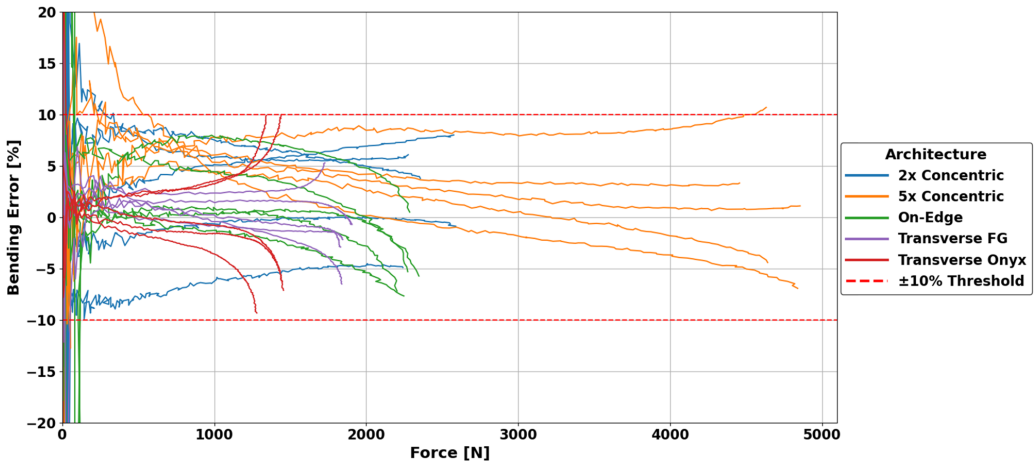


Figure 12. Bend error under compression for continuous fiberglass reinforced (CFGR) architectures obtained using digital image correlation (DIC). Dashed lines represents the ±10% bending error threshold.

3.2. Tensile Behavior

Tensile strength and Young's modulus results are presented in Figure 13A and 13B, respectively. The concentric ×5 architecture achieved the highest ultimate tensile strength at 451.59 MPa, followed by the on-edge architecture at 272.93 MPa and concentric ×2 at 204.02 MPa. Both the transverse FG and Onyx-only configurations exhibited much lower strengths, 24.88 MPa and 26.17 MPa, respectively. The overlapping 95% confidence intervals indicate that the observed difference between these mean values is small relative to the uncertainty associated with the measurements. This behavior is consistent with the limited fiber alignment with the loading direction and suggests that the addition of transverse fibers provides limited improvement in tensile strength. The Young's modulus showed a similar hierarchy, with concentric ×5 reaching 14.55 GPa, on-edge outperforming concentric ×2, and Onyx-only recording the lowest value of 0.79 GPa. While the transverse FG architecture did not meaningfully improve strength, it did yield greater stiffness compared to Onyx only. These results highlight the critical role of fiber orientation and build strategy in dictating tensile behavior, while also demonstrating that continuous fiberglass reinforcement may offer little benefit when fibers are poorly aligned with the loading direction. It should also be noted that this trend differs slightly from compression testing, emphasizing that CFGR architectures may perform differently under varying loading conditions.

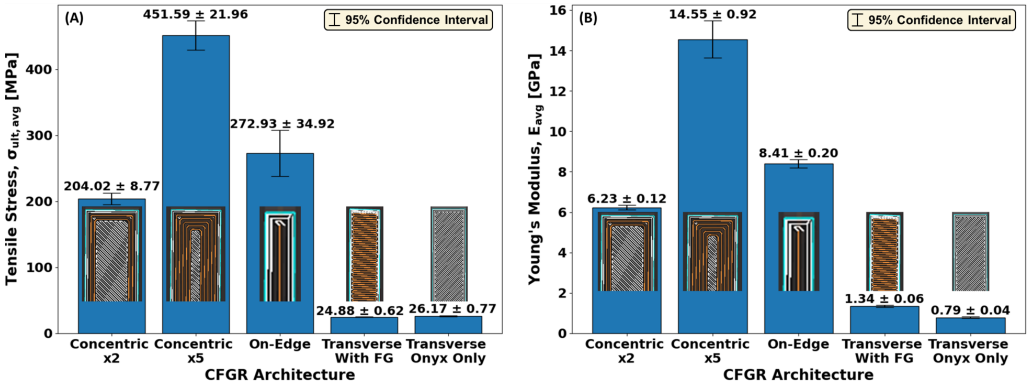


Figure 13. Tensile stress (**A**) and modulus (**B**) results for continuous fiberglass reinforced (CFGR) architectures.

3.3. Flexural Behavior

Flexural strength and modulus results are presented in Figure 14A and 14B, respectively. Among the tested architectures, the on-edge configuration exhibited the highest flexural strength at 116.03 MPa, followed by transverse FG at 50.53 MPa and Onyx only at 41.68 MPa. The performance of transverse FG and Onyx only was similar, as indicated by the overlap of their 95% confidence intervals, suggesting that FG reinforcement in the transverse orientation provided minimal benefit under flexural loading. The flexural modulus followed the same trend, with on-edge providing the greatest stiffness at 2.51 GPa, while transverse FG and Onyx-only recorded values of 1.31 GPa and 0.96 GPa, respectively. These results highlight the critical influence of build orientation on bending performance, with on-edge printing enabling more effective load transfer in flexion, while transverse CFGR reinforcement offered little advantage relative to the Onyx-only baseline. When considering the battery enclosure design and testing, it is important to note that although the case was printed with a concentric architecture along the *z*-axis, under cantilever loading the top and bottom walls effectively behave more like the on-edge configuration under flexion.

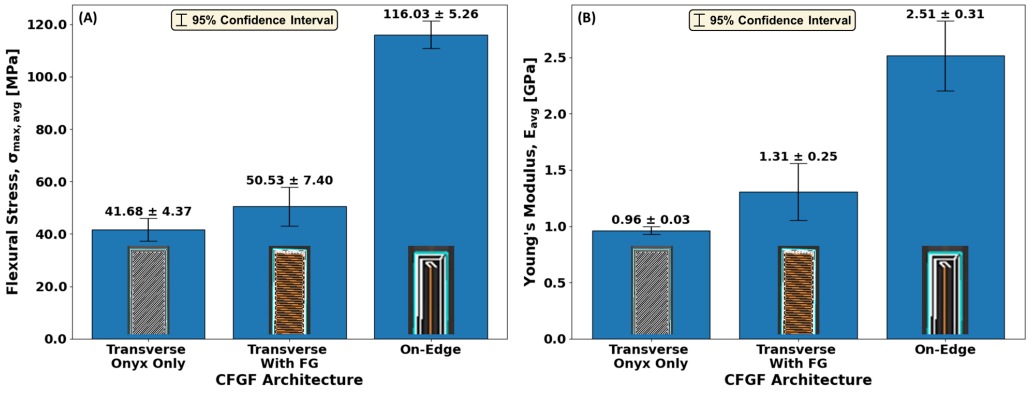


Figure 14. Flexure stress (**A**) and modulus (**B**) results for continuous fiberglass reinforcement (CFGR) architectures.

3.4. Cantilever Bend Fatigue

Before mechanical testing, candidate designs were evaluated using Markforged's simulation software to predict maximum deflection and minimum safety factor under cantilever loading. The target design was defined to accommodate the bend-induced deflection of aircraft wings, measured at approximately 7 mm at a distance of 304.8 mm from the fuselage or side of an X-57 aircraft [31]. The enclosure must be flexible enough to accommodate this deflection without failing. In the simulation, the left wall of the test module was fixed as an

anchor point, and a 100 N load was applied to the opposite end, replicating the boundary conditions illustrated in Figure 1.

To replicate the experimental boundary conditions, a slightly raised region was added to the simulated model to define the load application zone. Due to software limitations, only Onyx and continuous carbon fiber reinforcement could be modeled. The simulation predicted a minimum safety factor of 6.6 and a maximum deflection of 1.24 mm under a 100 N load. To extend these results to HSHT FG reinforcement, a rule of mixtures (RoM) analysis was performed using flexural properties listed in Table 1. Results indicated that HSHT FG exhibits 0.78 times the safety factor and 2.43 times the deflection of carbon fiber reinforcement. Based on these ratios, the adjusted safety factor and deflection for HSHT FG under 100 N were calculated as 5.13 and 3.01 mm, respectively. The yield load was then estimated as 513 N (safety factor × applied load). Accordingly, a 500 N target load was selected for simulation, producing a predicted maximum deflection of 15 mm at a safety factor of 1. An additional simulation at 85 N produced a 2.55 mm deflection and safety factor of 6.04. These results, summarized in Table 2, demonstrate that the HSHT FG-reinforced module is predicted to satisfy the design criterion of 7 mm deflection across its 304.8 mm length.

Table 2. Cantilever bend test simulation results for safety factor and deflection [mm] with applied loads of 85 N, 100 N, and 500 N. HSHT CFGR results are calculated from carbon fiber predictions based on the rule of mixtures. Yield load is also predicted.

Load [N]	Property	Carbon Fiber	HSHT Fiberglass
85	Safety Factor	7.76	6.04
	Deflection [mm]	1.05	2.55
100	Safety Factor	6.6	5.13
	Deflection [mm]	1.24	3.01
500	Safety Factor	1.32	1.03
	Deflection [mm]	6.18	15
Yield Load [N]:		660	513

Although the design criteria were satisfied, further analysis of fiber layering schemes and repeated simulations were conducted to explore potential optimizations. Table 3 summarizes the parameter combinations investigated along with the predicted safety factors and deflections. Design 1, representing the current enclosure configuration shown in Figure 3, served as the baseline. Design 2, composed entirely of Onyx, offered the lowest material cost but exhibited excessive deflection and lacked the thermo-mechanical benefits of HSHT FG reinforcement. Design 3 applied an isotropic fiber layering scheme, which increased safety factor while maintaining deflection, but at the expense of doubled print cost, longer build time, and slightly higher mass. Based on these predictions, Design 1 was selected as the most balanced configuration for cantilever bend testing, where opportunities for refinement could be informed by subsequent experimental results.

Bend-induced deflection of the battery enclosure was initially measured through preliminary bend testing, as shown in Figure 15. The preliminary testing was conducted to identify appropriate load levels for long-term fatigue testing and consisted of 4 loading cycles with an R-ratio of 0.1, corresponding to a load range of 10–100 N. The measured bend-induced deflection of the enclosure was 7.2 mm, providing a baseline for selecting long-term test loads.

Table 3. Module safety factor (SF), deflection (ΔX) [mm], and yield load (F_Y) [N] for several print parameter designs (Des.). Mat. = Material; LH = Layer height; M = Mass; PT = Print time; Conc. = Concentric; Iso. = Isotropic.

Des. [#]	Mat.	SF	ΔX [mm]	F_Y [N]	Fiber Layer	LH [µm]	M [kg]	PT [h]	Cost [$]
1	Onyx, HSHTFG	1.03	15	515	Conc.	125	1.1	156	654.39
2	Onyx	0.43	58.9	215	None	100	1.07	196	215.54
3	Onyx, HSHTFG	1.44	15	720	Iso.	125	1.12	196	1304.98

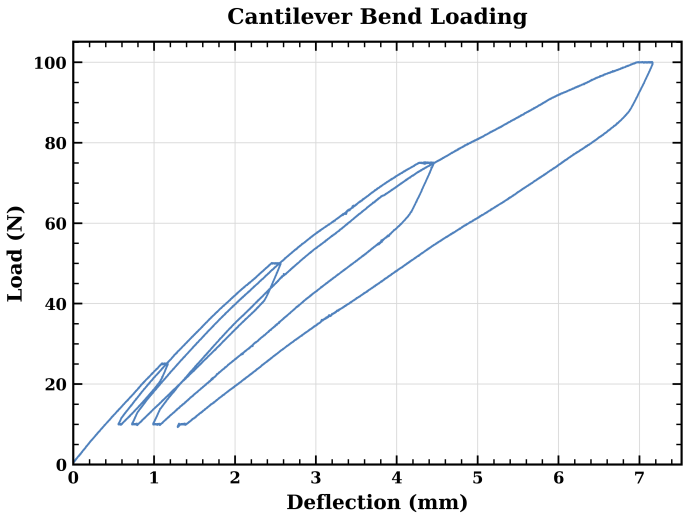


Figure 15. Cantilever bend loading cycles as a function of deflection.

Long-term cantilever bend fatigue testing was subsequently performed on the battery enclosure for 100 h under cyclic loading at 85 N with an R-ratio of 0.117. Figure 16A shows the loading cycles as a function of time for the final 5 h of testing, while Figure 16B presents the corresponding measured deflection over time. An initial deflection of 5.1 mm was observed with the first 85 N load. The maximum cumulative deflection of the enclosure reached 7.65 mm after 100 h, demonstrating that the module maintained structural integrity under extended cyclic loading. Evaluation of the mechanical response, accounting for enclosure length and damage evolution, indicated minimal cumulative deflection during testing without cracking, allowing the test to continue for 100 h (900 cycles). This performance is attributed to the engineered 3D-printed fiber-reinforced composite, including the design of fiber architecture and orientation relative to the loading direction. This 100 h cyclic test was designed as an initial feasibility study to evaluate whether the continuous fiber-reinforced enclosure could accommodate the target 7 mm deflection without catastrophic failure, rather than a full high-cycle aerospace qualification. Additionally, while in-service wing flexing occurs both above and below the neutral axis, testing was limited to unidirectional bending (below the neutral axis). Due to the geometric and structural symmetry of the enclosure, the mechanical response under reversed bending is expected to be equivalent. Additional work is required to characterize the high-cycle fatigue limit and fully establish long-term durability for flight qualification.

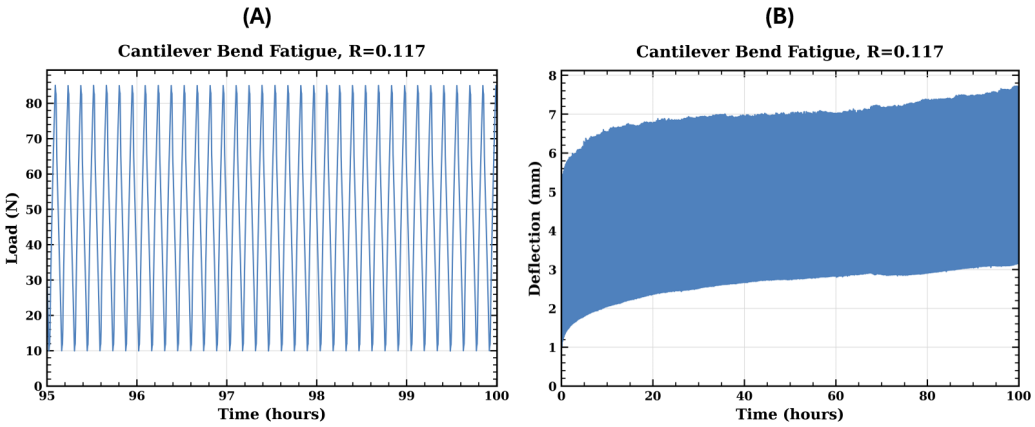


Figure 16. Cantilever bend fatigue test load cycles as a function of time for (**A**) the last 5 h and (**B**) the full 100 h of cyclic loading at 85 N, R 0.117.

These experimental results generally support the predictions from the Markforged simulation, indicating that the selected fiber architecture and print parameters provide sufficient flexibility to accommodate expected wing-induced deflections without compromising structural integrity. The measured deflection of 5.1 mm under the initial 85 N load was higher than the predicted value of 2.55 mm. This discrepancy may stem from assumptions and simplifications in the proprietary Eiger software, combined with the analytical rule-of-mixtures approximation. Nevertheless, the simulation provides a useful guide for evaluating trends and the relative effects of fiber architecture and print parameters on deflection. Under long-term cyclic loading, the measured deflection increased to 7.65 mm, which remained within the design criteria and supports the structural viability of the HSHT FG reinforced module, providing confidence in both the enclosure design and the cantilever bend fatigue methodology. Based on the mechanical test results, the casing met the required mechanical deflection criteria for compatibility with the X-57 wing structure.

In addition to the overall deflection trends, the physical response of the enclosure during and after testing was evaluated. The enclosure exhibited 3.1 mm of delayed elastic deflection immediately after 900 cycles (100 h), which fully recovered after 24 h of relaxation, confirming the absence of permanent plastic deformation. This recovery was likely supported by the continuous fiber reinforcement, which provided elastic restoring forces to the viscoelastic polymer matrix. However, local buckling of the thin side walls was observed during testing. This buckling occurred because the enclosure was evaluated in an open-face configuration without the heat sink or separator panels, representing a conservative, worst-case structural scenario. In the fully assembled system, the insertion of the rigid SG-200 fiberglass separator panels into the top and bottom grooves, along with the mechanically fastened rear heat sink, provides structural reinforcement. These components act as internal stiffeners that constrain lateral wall deformation, thereby mitigating local buckling and preventing the transfer of bending loads to any internal battery cells.

While the cantilever bending tests demonstrate the mechanical performance of the enclosure under the applied loading conditions, the suitability of the design for aircraft battery applications depends on additional system-level requirements. These include cell protection under representative dynamic loading and potential cell swelling, thermal management during normal operation and abnormal battery events, and durability under service-relevant environmental and mechanical conditions, including moisture exposure, temperature cycling, vibration, and fatigue. These requirements were not fully evaluated in the present study and warrant further investigation to establish the suitability of the enclosure for its intended aerospace application.

Accordingly, transitioning the current proof-of-concept toward practical aircraft battery applications will require further development to integrate system components, including thermal management materials, busbars, and electrical connectors, while balancing structural performance and mass. The material system should also be evaluated against applicable flammability and fire-safety requirements. Subsequent work should include ground-based structural, thermal, electrical, and environmental testing, followed by system-level validation as appropriate to the intended application. These steps would help establish the enclosure's suitability for integration into an aircraft battery system.

4. Conclusions

The design and mechanical evaluation of 3D-printed continuous fiberglass reinforced (CFGR) architectures, including a battery enclosure for advanced electric aircraft applications, were successfully conducted. The enclosure, fabricated using HSHT FG, was designed to provide structural integrity while minimizing weight. Cantilever bend fatigue testing demonstrated the enclosure could withstand repeated deflections of up to 7.65 mm over 100 h without cracking or permanent deformation, confirming that the module meets the preliminary mechanical flexibility requirements for compatibility with the X-57 wing structure.

Simulation-based design, using Markforged's proprietary software, allowed the prediction of maximum deflection and safety factors, guiding fiber architecture, layering schemes, and print parameters. Although constrained by the limitations of a black-box simulation environment, this integrated design–simulation–testing workflow enabled systematic exploration of process–structure–property relationships and informed design choices to optimize mechanical performance.

The results highlight the critical role of fiber orientation and architecture in determining mechanical performance, from coupon-level testing to full enclosure response under cantilever loading. This study demonstrates that AM with CFGR can produce lightweight, structurally reliable battery enclosures capable of meeting rigorous mechanical demands. The methodology presented provides a framework for future development of multi-functional components in electric and hybrid-electric aircraft, enabling the combination of structural optimization with additional performance criteria such as thermal management and impact resistance. However, full suitability for use in an aircraft remains subject to further multi-functional validation, as service-relevant conditions such as thermal management, integrated battery-cell behavior, and dynamic loading need experimental evaluation. In future work, a thermal management system will be integrated with the battery enclosure to evaluate performance under thermal runaway events, further advancing the design toward safe and robust operational use.

Author Contributions: Conceptualization, M.R., A.A., and M.S.; methodology, M.R. and A.A.; investigation, M.R. and A.A.; data analysis, M.R. and A.A.; software, M.R.; writing—original draft preparation, M.R.; writing—review and editing, M.R., M.S., and A.A.; supervision, A.A. and M.S.; funding acquisition, A.A. All authors have read and agreed to the published version of the manuscript.

Funding: This research was primarily supported by the NASA Transformational Tools and Technologies (TTT) project under the Battery Thermal Management Project and the Integrated Methods and Research (IMR) Project, with additional support from the Aeronautics Flight Accelerator initiative.

Data Availability Statement: The raw data supporting the conclusions of this article will be made available by the authors on request.

Acknowledgments: The authors would like to thank Daniel Gorican for assistance with mechanical testing. Special thanks is given to the NASA Transformational Tools and Technologies (TTT) project

and the Integrated Methods and Research (IMR) Project for their primary support, as well as the Aeronautics Flight Accelerator (AFA) initiative.

Conflicts of Interest: The authors declare no conflicts of interest. The funders had no role in the design of the study; in the collection, analyses, or interpretation of data; in the writing of the manuscript; or in the decision to publish the results.

References

1. Burd, J.T.J.; Moore, E.A.; Ezzat, H.; Kirchain, R.; Roth, R. Improvements in electric vehicle battery technology influence vehicle lightweighting and material substitution decisions. *Appl. Energy* **2021**, *283*, 116269. [CrossRef]
2. Xiong, Y.; Pan, Y.; Wu, L.; Liu, B. Effective weight-reduction-and crashworthiness-analysis of a vehicle's battery-pack system via orthogonal experimental design and response surface methodology. *Eng. Fail. Anal.* **2021**, *128*, 105635. [CrossRef]
3. Cheng, P.; Peng, Y.; Li, S.; Rao, Y.; Le Duigou, A.; Wang, K.; Ahzi, S. 3D printed continuous fiber reinforced composite lightweight structures: A review and outlook. *Compos. Part B Eng.* **2023**, *250*, 110450. [CrossRef]
4. Li, N.; Link, G.; Wang, T.; Ramopoulos, V.; Neumaier, D.; Hofele, J.; Walter, M.; Jelonnek, J. Path-designed 3D printing for topological optimized continuous carbon fibre reinforced composite structures. *Compos. Part B Eng.* **2020**, *182*, 107612. [CrossRef]
5. Goh, G.D.; Yap, Y.L.; Agarwala, S.; Yeong, W.Y. Recent progress in additive manufacturing of fiber reinforced polymer composite. *Adv. Mater. Technol.* **2019**, *4*, 1800271. [CrossRef]
6. Gibson, I.; Rosen, D.; Stucker, B.; Khorasani, M. *Additive Manufacturing Technologies*, 3 ed.; Springer: Cham, Switzerland, 2021; Volume 17. [CrossRef]
7. Popescu, D.; Zapciu, A.; Amza, C.; Baciu, F.; Marinescu, R. FDM process parameters influence over the mechanical properties of polymer specimens: A review. *Polym. Test.* **2018**, *69*, 157–166. [CrossRef]
8. Ranaiefar, M.; Singh, M.; Salem, J.A.; Halbig, M.C. Compressive Properties of Additively Manufactured Metal-Reinforced PLA and ABS Composites. *Polymers* **2024**, *16*, 2008. [CrossRef]
9. Dimitrellou, S.; Iakovidis, I.; Psarianos, D.R. Mechanical characterization of polylactic acid, polycarbonate, and carbon fiber-reinforced polyamide specimens fabricated by fused deposition modeling. *J. Mater. Eng. Perform.* **2024**, *33*, 3613–3626. [CrossRef]
10. Podsiadły, B.; Skalski, A.; Rozpiórski, W.; Słoma, M. Are we able to print components as strong as injection molded?—Comparing the properties of 3D printed and injection molded components made from ABS thermoplastic. *Appl. Sci.* **2021**, *11*, 6946. [CrossRef]
11. Ahn, S.H.; Montero, M.; Odell, D.; Roundy, S.; Wright, P.K. Anisotropic material properties of fused deposition modeling ABS. *Rapid Prototyp. J.* **2002**, *8*, 248–257. [CrossRef]
12. Torrado, A.R.; Roberson, D.A. Failure analysis and anisotropy evaluation of 3D-printed tensile test specimens of different geometries and print raster patterns. *J. Fail. Anal. Prev.* **2016**, *16*, 154–164. [CrossRef]
13. Es-Said, O.S.; Foyos, J.; Noorani, R.; Mendelson, M.; Marloth, R.; Pregger, B.A. Effect of layer orientation on mechanical properties of rapid prototyped samples. *Mater. Manuf. Processes* **2000**, *15*, 107–122. [CrossRef]
14. Sood, A.K.; Ohdar, R.K.; Mahapatra, S.S. Parametric appraisal of mechanical property of fused deposition modelling processed parts. *Mater. Des.* **2010**, *31*, 287–295. [CrossRef]
15. Lambiase, F.; Liparoti, S.; Pace, F.; Scipioni, S.I.; Paoletti, A. A multidisciplinary approach to investigate the influence of process parameters on interlayer adhesion in material extrusion additive manufacturing. *Int. J. Adv. Manuf. Technol.* **2024**, *133*, 5553–5570. [CrossRef]
16. Morettini, G.; Palmieri, M.; Capponi, L.; Landi, L. Comprehensive characterization of mechanical and physical properties of PLA structures printed by FFF-3D-printing process in different directions. *Prog. Addit. Manuf.* **2022**, *7*, 1111–1122. [CrossRef]
17. Ranaiefar, M.; Singh, M.; Halbig, M.C. Additively Manufactured Carbon-Reinforced ABS Honeycomb Composite Structures and Property Prediction by Machine Learning. *Molecules* **2024**, *29*, 2736. [CrossRef]
18. Li, J.; Durandet, Y.; Huang, X.; Sun, G.; Ruan, D. Additively manufactured fiber-reinforced composites: A review of mechanical behavior and opportunities. *J. Mater. Sci. Technol.* **2022**, *119*, 219–244. [CrossRef]
19. Handwerker, M.; Wellnitz, J.; Marzbani, H. Review of mechanical properties of and optimisation methods for continuous fibre-reinforced thermoplastic parts manufactured by fused deposition modelling. *Prog. Addit. Manuf.* **2021**, *6*, 663–677. [CrossRef]
20. Blok, L.G.; Longana, M.L.; Yu, H.; Woods, B.K. An investigation into 3D printing of fibre reinforced thermoplastic composites. *Addit. Manuf.* **2018**, *22*, 176–186. [CrossRef]
21. Justo, J.; Távara, L.; García-Guzmán, L.; París, F. Characterization of 3D printed long fibre reinforced composites. *Compos. Struct.* **2018**, *185*, 537–548. [CrossRef]
22. Caminero, M.; Chacón, J.; García-Moreno, I.; Rodríguez, G. Impact damage resistance of 3D printed continuous fibre reinforced thermoplastic composites using fused deposition modelling. *Compos. Part B Eng.* **2018**, *148*, 93–103. [CrossRef]

23. Davis, J.R., Ed. Properties and Selection: Nonferrous Alloys and Special-Purpose Materials. In *ASM Handbook*, 10th ed.; ASM International: Materials Park, OH, USA, 1990; Volume 2.
24. Markforged Datasheets. Available online: https://markforged.com/datasheets (accessed on 5 September 2025).
25. Mulholland, T.; Goris, S.; Boxleitner, J.; Osswald, T.A.; Rudolph, N. Fiber Orientation Effects in Fused Filament Fabrication of Air-Cooled Heat Exchangers. *JOM* **2018**, *70*, 298–302. Correction in *JOM* **2018**, *70*, 2765. [CrossRef]
26. Qiu, J. *Multifunctional Multiscale Composites: Processing, Modeling and Characterization*; The Florida State University: Tallahassee, FL, USA, 2008.
27. Ibrahim, Y.; Elkholy, A.; Schofield, J.S.; Melenka, G.W.; Kempers, R. Effective thermal conductivity of 3D-printed continuous fiber polymer composites. *Adv. Manuf. Polym. Compos. Sci.* **2020**, *6*, 17–28. [CrossRef]
28. *ASTM D6641/D6641M-23*; Standard Test Method for Compressive Properties of Polymer Matrix Composite Materials Using a Combined Loading Compression (CLC) Test Fixture. ASTM International: West Conshohocken, PA, USA, 2023.
29. *ASTM D3039/D3039M-17*; Standard Test Method for Tensile Properties of Polymer Matrix Composite Materials. ASTM International: West Conshohocken, PA, USA, 2017.
30. *ASTM D790-17*; Standard Test Methods for Flexural Properties of Unreinforced and Reinforced Plastics and Electrical Insulating Materials. ASTM International: West Conshohocken, PA, USA, 2017.
31. Miller, E.J.; Li, W.W.; Jordan, A.; Lung, S.F. X-57 Wing Structural Load Testing. In Proceedings of the AIAA Aviation 2020 Forum, Virtual Event, 15–19 June 2020; p. 3090. [CrossRef]

Disclaimer/Publisher's Note: The statements, opinions and data contained in all publications are solely those of the individual author(s) and contributor(s) and not of MDPI and/or the editor(s). MDPI and/or the editor(s) disclaim responsibility for any injury to people or property resulting from any ideas, methods, instructions or products referred to in the content.